nature research

https://doi.org/10.1038/s41929-020-00526-5

Supplementary information

A spatially orthogonal hierarchically porous acid–base catalyst for cascade and antagonistic reactions

In the format provided by the authors and unedited

Supplementary Information

A spatially orthogonal hierarchically porous acid-base catalyst for cascade and antagonistic reactions

Mark A. Isaacs,[1,2] Christopher M.A. Parlett,[3,4,5] Neil Robinson,[6] Lee J. Durndell,[7] Jinesh Manayil,[8] Simon K. Beaumont,[9] Shan Jiang,[10] Nicole S. Hondow,[11] Alexander C. Lamb,[12] Deshetti Jampaiah,[12] Michael L. Johns,[6] Karen Wilson[12]* and Adam F. Lee[12]*

[1]Department of Chemistry, University College London, London WC1H 0AJ, UK
[2]HarwellXPS, Research Complex at Harwell, Rutherford Appleton Laboratories, Didcot OX11 0FA, UK
[3]Department of Chemical Engineering and Analytical Science, University of Manchester, Manchester M13 9PL, UK
[4]University of Manchester at Harwell, Diamond Light Source, Harwell Science and Innovation Campus, Didcot OX11 0DE, UK.
[5]Diamond Light Source, Harwell Science and Innovation Campus, Didcot OX11 0DE, UK.
[6]Department of Chemical Engineering, University of Western Australia, Perth WA6009, Australia
[7]School of Geography, Earth and Environmental Sciences, University of Plymouth, Plymouth PL4 8AA, UK
[8]European Bioenergy Research Institute, Aston University, Birmingham B4 7ET, UK
[9]Department of Chemistry, Durham University, Durham DH1 3LE, UK
[10]School of Physical Science and Technology, ShanghaiTech University, Shanghai, China
[11]School of Chemical and Process Engineering, University of Leeds, Leeds LS2 9JT, UK
[12]School of Science, RMIT University, Melbourne VIC3000, Australia

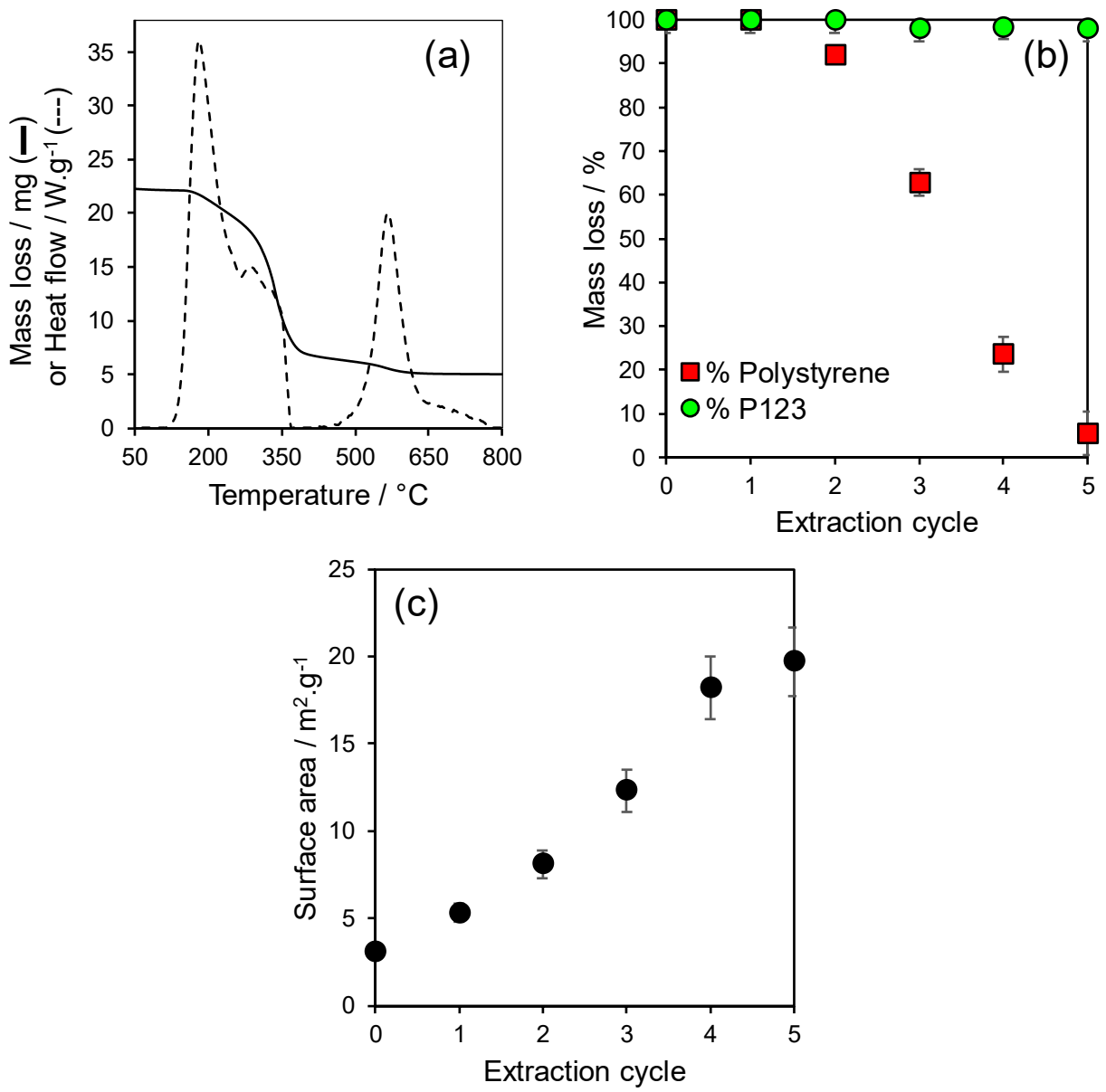

Supplementary Figure 1: (a) Thermogram of Mg-functionalised P123/polystyrene templated SBA-15, and (b) corresponding thermogravimetric analysis and (c) BET surface areas as a function of toluene cold extraction cycle. Template combustion range for analysis: 150-300 °C for P123, and 300-400 °C for polystyrene nanospheres (the 600 °C mass loss at is attributed to silica dehydroxylation). Error bars represent S.D. of the mean (n=2).

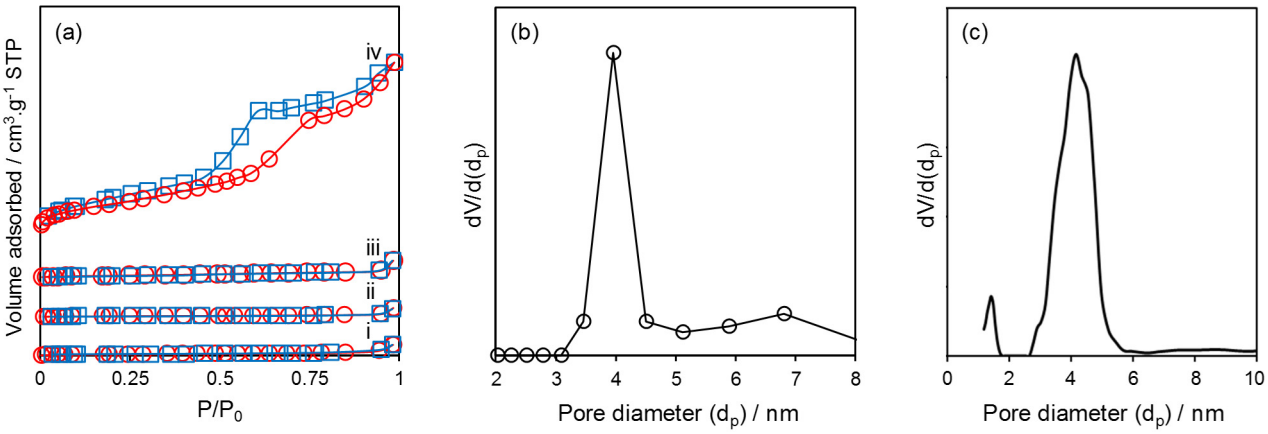

Supplementary Figure 2: (a) N_2 adsorption-desorption isotherms of Mg functionalised P123/polystyrene templated SBA-15 following (i) toluene extraction of polystyrene nanosphere, (ii) zirconia functionalisation of macropores, (iii) sulphation of macropores, and (iv) calcination to form spatially orthogonal, hierarchical sulfated zirconia (SZ) macroporous-MgO mesoporous SBA-15. Pore size distributions from (b) BJH and (c) DFT analysis of calcined spatially orthogonal, hierarchical SZ macroporous-MgO mesoporous SBA-15 (a, iv).

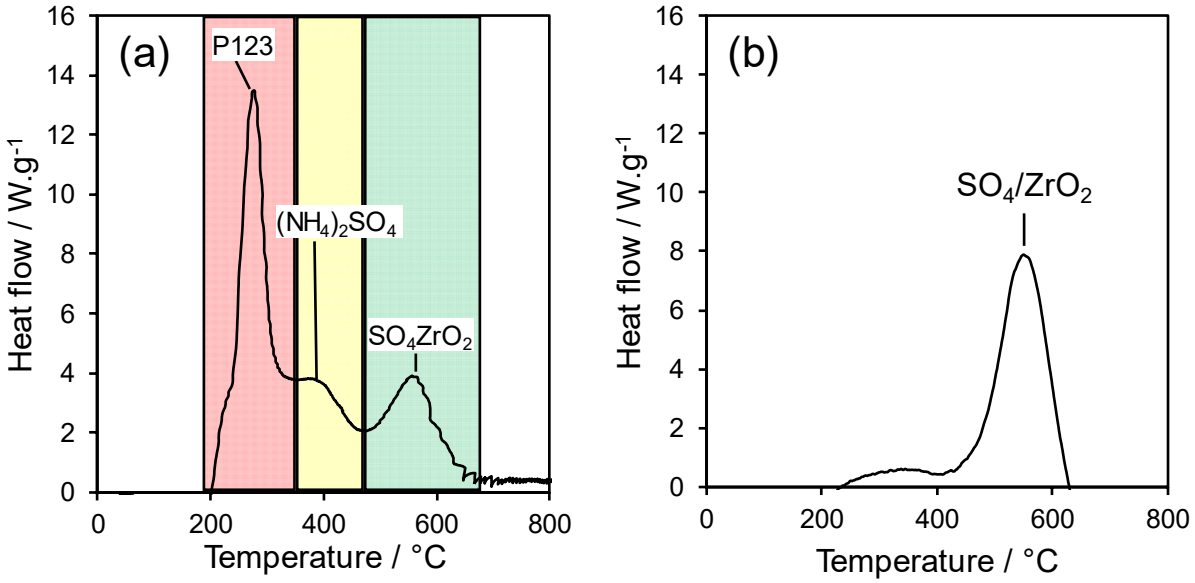

Supplementary Figure 3: Thermograms under flowing O_2/N_2 of (a) surfactant templated, Mg and Zr functionalised organic-silica framework, and after (b) calcination to form SZ/MgO/MM-SBA-15. Regions assigned based on thermograms of reference compounds.

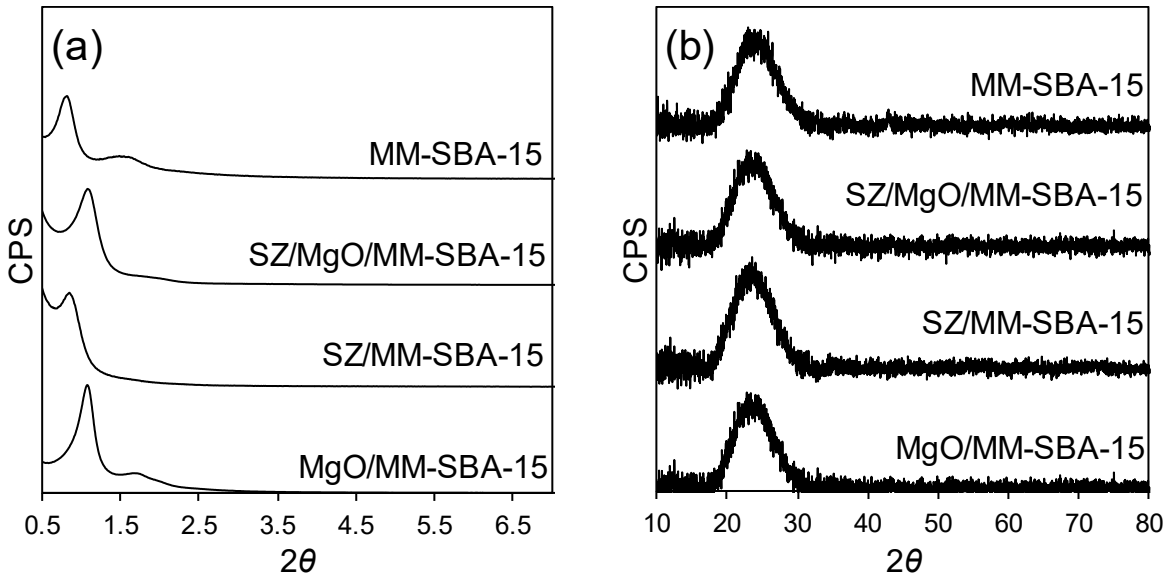

Supplementary Figure 4: (a) Low-angle and (b) wide-angle powder XRD of MM-SBA-15 materials. Low angle XRD diffractograms exhibit d_{10} reflections characteristic of ordered mesoporous channels possessing *p6mm* symmetry within SBA-15 silica. Wide angle XRD patterns indicate no magnesium or zirconium containing crystalline phases, evidencing both elements are present in highly dispersed forms.

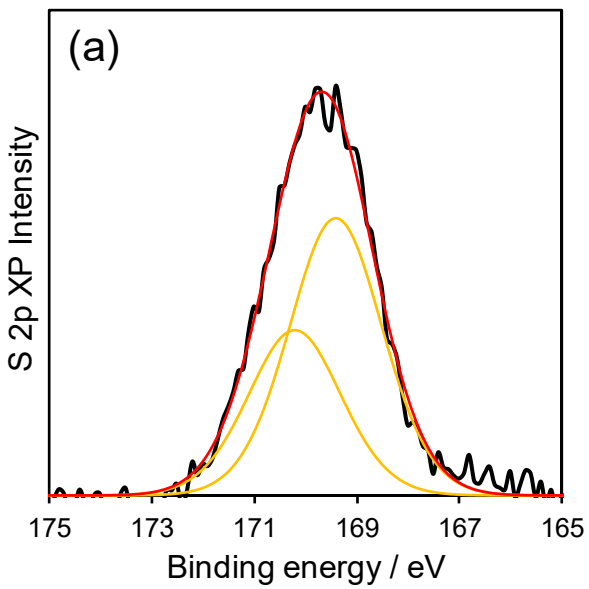

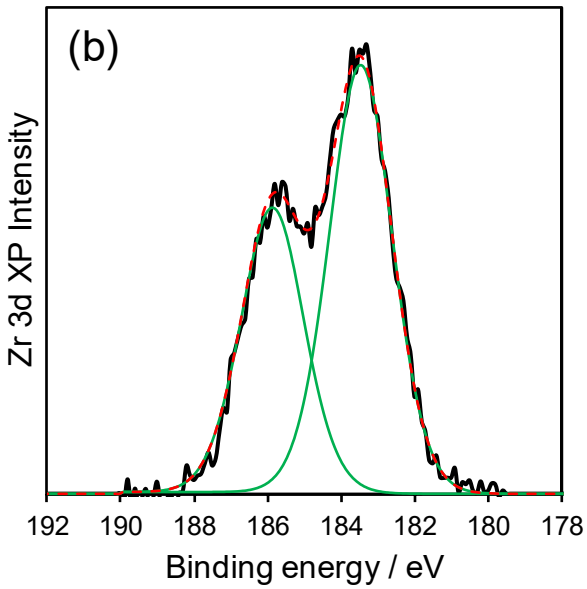

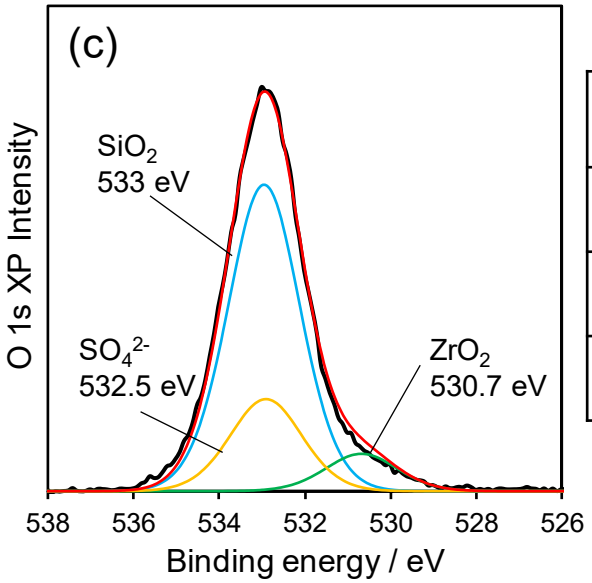

(d)

O 1s component	O / %	O / atom%	**X** (S, Zr, or Si) / atom%	O:**X** atomic ratio
S(O)	21.1	9.5	2.5	3.8
Zr(O)	8.8	4.0	2.0	2.0
Si(O)	70.3	31.7	16.6	1.9

Supplementary Figure 5: (a) S 2p, (b) Zr 3d, and (c) O 1s XP spectra of SZ/MgO/MM-SBA-15, and (d) fitted O 1s environments from (c) and corresponding O:X atomic ratios (where X = S, Zr or Si). Note that the S:Zr atomic ratio of 1.2 corresponds to almost stoichiometric SO_4/ZrO_2. S $2p_{3/2}$ (169.3 eV) and Zr $3d_{5/2}$ (183.3 eV) binding energies, and associated O 1s binding energies of sulfate (532.5 eV) and zirconia (530.7 eV) fitted components, are all consistent with SO_4/ZrO_2.[1,2]

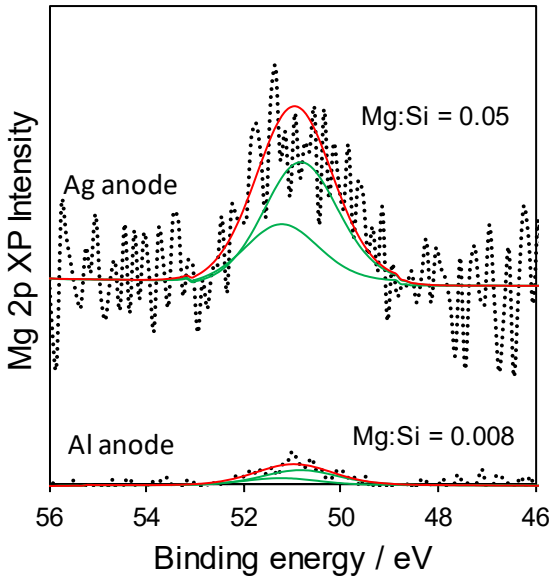

Supplementary Figure 6: High resolution Mg 2p XP spectra of SZ/MgO/MM-SBA-15 using (a) Ag (2984.3 eV) and (b) Al (1486.6 eV) K_α excitation sources. Spectra acquired using silver and aluminium excitation sources were normalised to obtain a common adventitious carbon signal intensity.

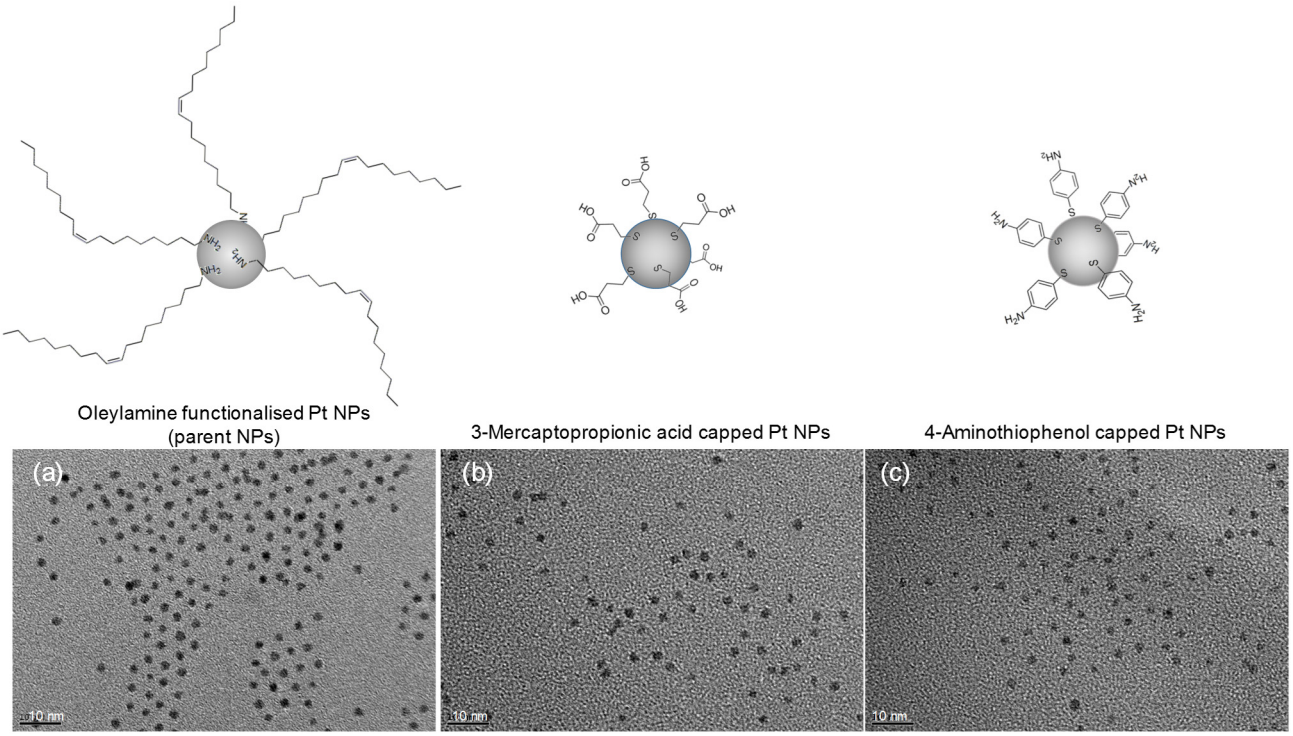

Supplementary Figure 7: Bright-field TEM micrographs of (a) oleylamine, (b) 3-mercaptopropionic acid, and (c) 4-aminothiophenol functionalised Pt nanoparticles (NPs). 3-mercaptopropionic acid and 4-aminothiophenol introduced by ligand-exchange with parent (oleylamine functionalised) Pt NPs.

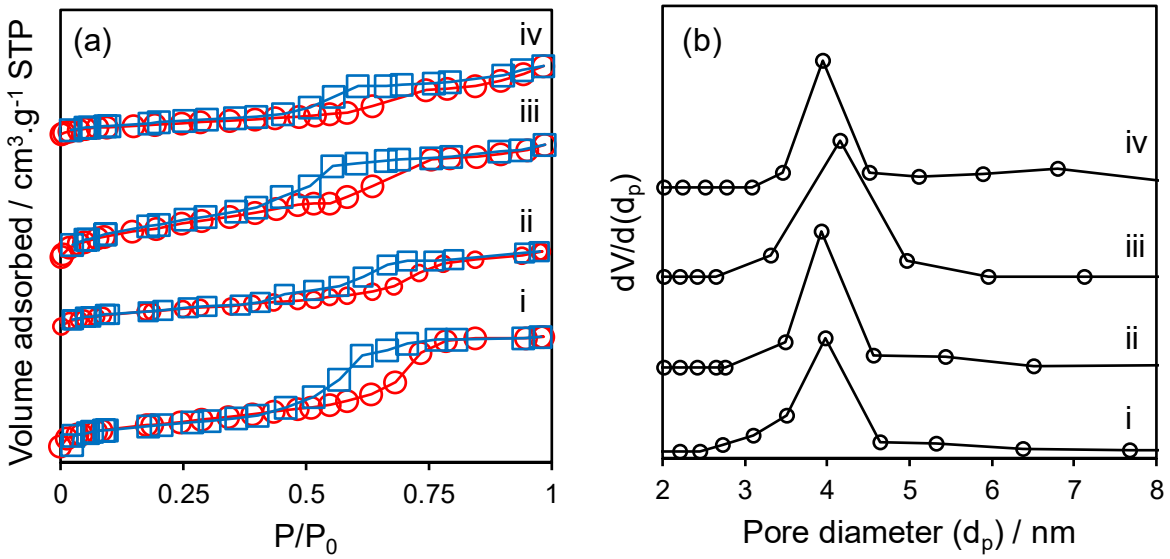

Supplementary Figure 8: (a) N_2 adsorption isotherms and (b) BJH pore-size distributions of (i) MM-SBA-15, (ii) MgO/MM-SBA-15, (iii) SZ/MM-SBA-15 and (iv) SZ/MgO/MM-SBA-15. All materials exhibit type-IV isotherms with H1 hysteresis characteristic of mesoporous SBA-15, and a common mesopore diameter.

Supplementary Table 1: Textural properties of MM-SBA-15 materials.

	Total surface area[a] / $m^2.g^{-1}$	Pore diameter[b] / nm	Total pore volume / $cm^3.g^{-1}$	Mesopore volume / $cm^3.g^{-1}$
SZ/MgO/MM-SBA-15	350	4	0.4	0.1
SZ/MM-SBA-15	385	4	0.5	0.2
MgO/MM-SBA-15	365	4	0.5	0.1

[a]BET, and [b]BJH.

Supplementary Table 2: Elemental compositions of MM-SBA-15 materials.

	S[a] / wt%	Zr[b] / wt%	Mg[b] / wt%
SZ/MgO/MM-SBA-15	1.20 ± 0.05	2.02 ± 0.03	0.98 ± 0.03
MgO/MM-SBA-15	0	0	1.15 ± 0.02
SZ/MM-SBA-15	1.03 ± 0.05	1.89 ± 0.03	0.00

[a]CHNS, and [b]ICP-OES.

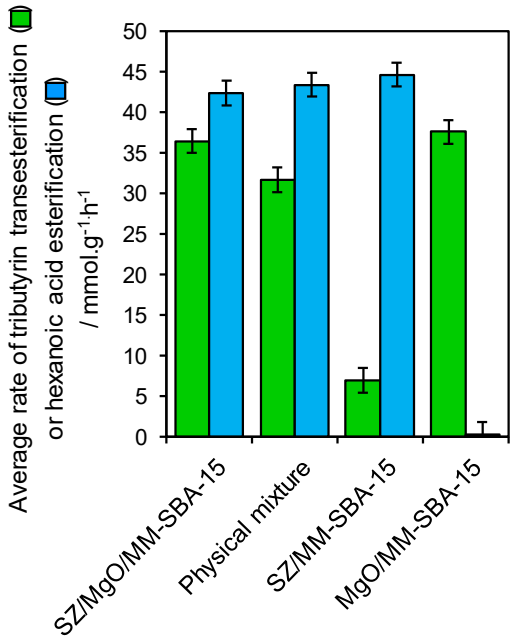

Supplementary Figure 9: Hexanoic acid esterification and tributyrin transesterification in methanol. Error bars represent S.D. of the mean (n=3). Reaction conditions: 25 mg catalyst (except for physical mixture where 25 mg of each monofunctional catalyst was used), 5 mmol tributyrin or 5 mmol hexanoic acid, 60 cm^3 methanol, 0.1 mmol dihexylether as an internal standard, 90 °C under air (autogeneous pressure).

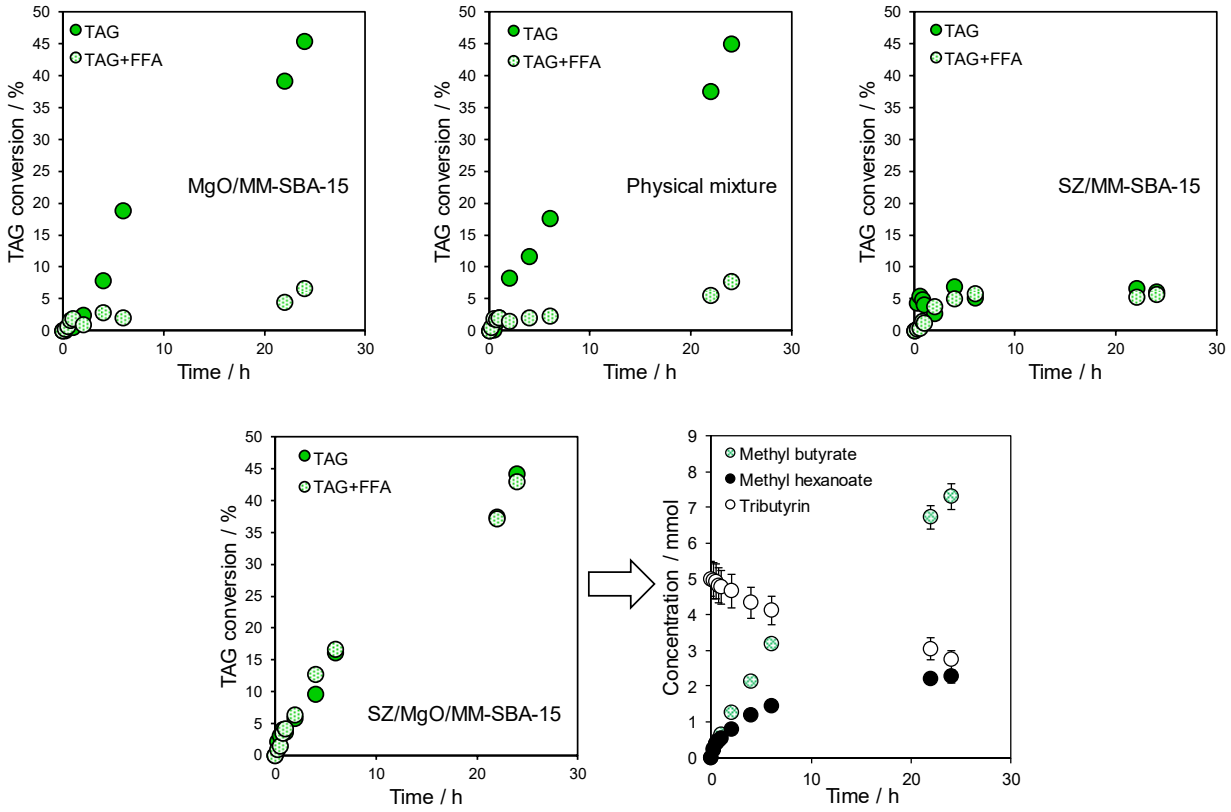

Supplementary Figure 10: Catalytic tributyrin transesterification with methanol in the presence of hexanoic acid. Reaction conditions: 25 mg of catalyst (except for physical mixture where 25 mg of each monofunctional catalyst was used), 5 mmol tributyrin or a mixture of 5 mmol tributyrin and 5 mmol hexanoic acid, 60 cm^3 methanol, 0.1 mmol dihexylether as an internal standard, 90 °C under air (autogenous pressure). Error bars represent S.D. of the mean (n=3).

Supplementary Table 3: Catalytic performance for tributyrin transesterification with methanol, hexanoic esterification with methanol, and tributyrin transesterification with methanol in the presence of hexanoic acid.[a]

Catalyst	Average rate[b] / mmol.g_{cat}^{-1}.h^{-1}	24 h conversion / %	24 h FAME yield (unoptimised) / %
	Tributyrin transesterification		
SZ/MgO/MM-SBA-15	37	44	44 (methyl butyrate)
Physical mixture	32	45	45 (methyl butyrate)
MgO/MM-SBA-15	38	46	46 (methyl butyrate)
SZ/MM-SBA-15	8	6	6 (methyl butyrate)
	Hexanoic acid esterification		
SZ/MgO/MM-SBA-15	42	53	53 (methyl hexanoate)
Physical mixture	44	60	60 (methyl hexanoate)
SZ/MM-SBA-15	45	62	62 (methyl hexanoate)
MgO/MM-SBA-15	0	5	5 (methyl hexanoate)
	Tributyrin transesterification + hexanoic acid		
SZ/MgO/MM-SBA-15	37	43	43 (methyl butyrate)
Physical mixture	2	5	5 (methyl butyrate)
MgO/MM-SBA-15	2	7	7 (methyl butyrate)
SZ/SBA-15	4	6	6 (methyl butyrate)

[a]Reaction conditions: 25 mg catalyst (except for physical mixture where 25 mg of each monofunctional catalyst was used), 5 mmol tributyrin (or 5 mmol hexanoic acid, or a mixture of 5 mmol tributyrin and 5 mmol hexanoic acid), 60 cm^3 methanol, 0.1 mmol dihexylether as an internal standard, 90 °C under air (autogenous pressure).
[b]Calculated over first 30 min of reaction.

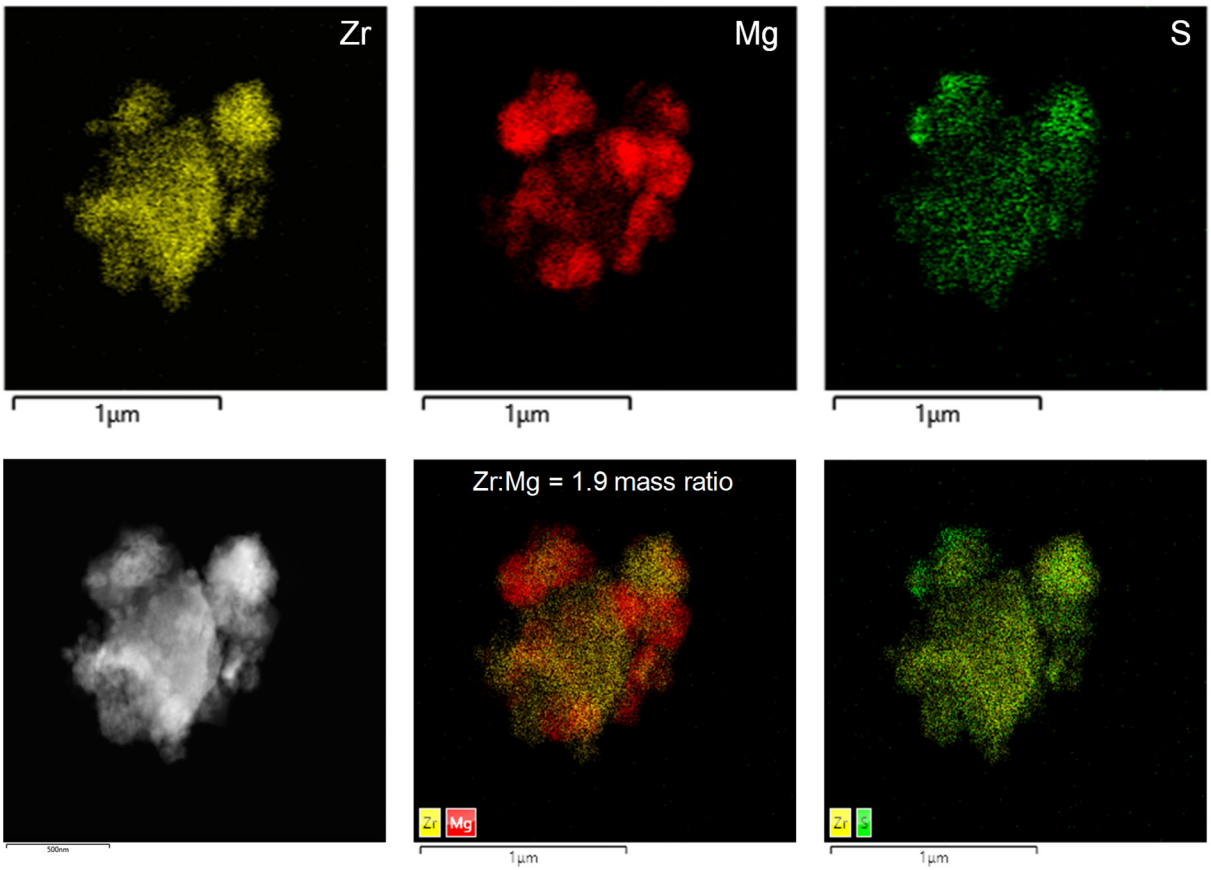

Supplementary Figure 11: (bottom left) HAADF-STEM image of 34 wt% MgO/SZ catalyst and corresponding EDX elemental maps evidencing co-location of randomly distributed MgO at the surface of SZ particles.

Supplementary Discussion: Low magnetic field ^{1}H NMR relaxation correlation measurements.

Background:

In the present work we performed a series of low magnetic field ^{1}H NMR relaxation correlation measurements on an unfunctionalised MM-SBA-15 framework in excess water. The longitudinal (T_1) and transverse (T_2) nuclear spin relaxation properties of spin-bearing liquids confined to porous media are typically described in terms of biphasic fast-exchange between an adsorbed surface layer and bulk-liquid towards the centre of the pores.[3] The observed relaxation rates are interpreted as a weighted average of the two components, such that[4]

$$\frac{1}{T_{1,obs}} = \frac{1-P}{T_{1,bulk}} + \frac{P}{T_{1,bulk}}, \quad \textbf{(1)}$$

$$\frac{1}{T_{2,obs}} = \frac{1-P}{T_{2,bulk}} + \frac{P}{T_{2,bulk}} + \frac{1}{T_{2,D}}. \quad \textbf{(2)}$$

Here, $T_{i,obs}$ are the observed relaxation characteristics (with $i = \{1,2\}$), while $T_{i,bulk}$ and $T_{i,surf}$ are the relaxation time constants in the unrestricted bulk and within the adsorbed surface layer, respectively. $T_{2,D}^{-1}$ describes additional transverse nuclear spin relaxation which may occur as a result of diffusion through regions

of magnetic field inhomogeneity throughout the pore structure (so-called internal gradients) during the measurement of T_2.[5,6] These internal gradients arise due to unfavourable magnetic susceptibility contrast effects at the solid-liquid interface; as the strength of such effects scales with applied magnetic field strength,[5] this term may be considered negligible under low-field conditions. T_1 relaxation is known to be independent of such phenomena.[7] The term P describes the population of the adsorbed surface layer and is given by $P = \delta S/V$, wherein δ is the layer thickness and S/V describes the surface-to-volume ratio of the pore structure.[8] Given the sensitivity of T_1 and T_2 to molecular dynamics,[9] it is often possible to simplify **Supplementary Equations 1** and **2**. In particular, the influence of adsorption interactions at the solid-liquid interface mean that $T_{i,bulk} \gg T_{i,surf}$.[3] Assuming S/V is large, these expressions may therefore be simplified to[4]

$$\frac{1}{T_{i,obs}} \approx \frac{S}{V}\frac{\delta}{T_{i,surf}}, \qquad \textbf{(3)}$$

highlighting the sensitivity of measured nuclear spin relaxation time constants to pore size (via the term S/V). The constant of proportionality between relaxation characteristics and pore size $\delta/T_{i,surf}$ is known as the surface relaxivity.[8] In the present experiments water was found to exhibit optimal transverse surface relaxivity characteristics in terms of resolving the different pore structures present within the hierarchical MM-SBA-15 material, and so was selected as our probe liquid.

The NMR pulse sequence for $T_2 - T_2$ relaxation-exchange measurements is illustrated in **Supplementary Figure 12** and described in detail elsewhere.[10-12] Upon varying the parameters n_A and n_B independently a two-dimensional (2D) ($n_A \times n_B$) data decay surface is acquired by recording the echo magnitudes exhibited by the second echo train within the pulse sequence (white data point in **Supplementary Figure 12**); as the two dimensions of this data surface decay according to T_{2A} and T_{2B}, respectively, a 2D distribution of T_{2A} and T_{2B} relaxation times may be acquired via an appropriate inversion of the experimental data. The acquired NMR signal $S(n_{A,B}t_e, T_{2A,B})$ is described according to the 2D Fredholm integral equation,[13]

$$S(n_{A,B}t_e, T_{2A,B}) = S_0 \iint K(n_{A,B}t_e, T_{2A,B})\, F(T_{2A,B})\, d\log_{10}(T_{2A,B}) + \epsilon(n_{A,B}t_e). \qquad \textbf{(4)}$$

Here the Kernel function

$$K(n_{A,B}t_e, T_{2A,B}) = \exp\left(\frac{-n_A t_e}{T_{2A}}\right)\exp\left(\frac{-n_B t_e}{T_{2B}}\right) \qquad \textbf{(5)}$$

describes the expected relaxation behaviour of the acquired data, while $\epsilon(n_{A,B}t_e)$ is the experimental noise (assumed Gaussian with zero mean); the echo time t_e and parameters n_A and n_B are illustrated in **Supplementary Figure 12**. $F(T_{2A,B})$ is the desired 2D distribution of T_{2A} and T_{2B} time constants and is obtained via an inverse Laplace transform of the acquired 2D NMR data.[13] As such inversions are ill-posed (i.e. there exists an infinite number of $F(T_{2A,B})$ distributions which satisfy any given data set) it is necessary to impose restrictions on the optimisation (or regularisation) process used to invert our data: the inverted distribution is typically biased to be smooth, non-negative, and lie within a certain range of output parameters.[14] The T_{2A} (indirect) dimension was encoded using 32 logarithmically spaced n_A values between 2 and 12000, while the T_{2B} (direct) dimension was obtained by recording the magnitude of n_B = 12000 spin echoes. The 90° and 180° radio frequency pulse lengths were 12.5 µs and 25.0 µs, respectively, and a constant echo time of t_e = 250 µs was employed throughout. Measurements were obtained using multiple t_{mix} times between 50 ms and 2.5 s, during which a homospoil gradient was applied to remove any remaining coherent transverse magnetisation. Measurements were averaged over up to 40 repeat scans, taking up to 5 h to complete; the recycle delay was 3 $\times T_1$ of the slowest relaxing component and the signal-to-noise ratio (SNR) of the acquired data ranged from

40 to 600 depending on the t_{mix} value employed. In each case the resulting data surface was reduced from a (32 × 12000) array to a symmetrical (32 × 32) array by only retaining data from direct encoding times ($n_B t_e$) that corresponded with the 32 indirect encoding times ($n_A t_e$) employed.[11] The data were then inverted via Tikhonov regularisation;[13] the inversion codes used in this work were first implemented by Mitchell et al.[12,15] The resulting 2D distributions were limited to 200 × 200 values and the two dimensions bound within the range $\{10^{-4}, 10^{1}\}$s. A constant smoothing parameter was maintained across all data sets and was determined from analysis of our t_{mix} = 50 ms data (highest SNR) according to the generalised cross-validation (GCV) method.[16] As such distributions are likely to exhibit artefacts associated with the inversion of low SNR data,[14] we stress that we have attempted to avoid over-analysis of low intensity peaks or eccentric peak shapes, and instead comment only on peak structures which are clear, unambiguous and physically reasonable.

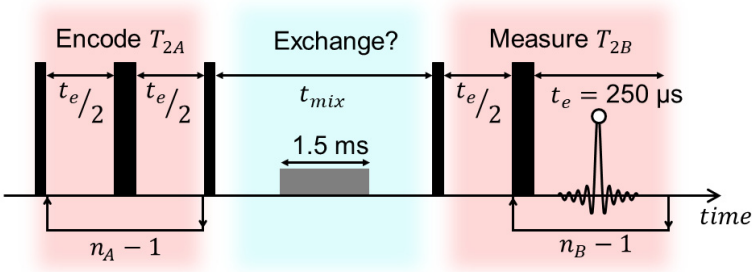

Supplementary Figure 12. NMR pulse sequence for $T_2 - T_2$ relaxation-exchange measurements. Thick and thin bars represent 180° and 90° radio frequency pulses, respectively, while the grey shaded area indicates the homospoil gradient applied during the mixing time t_{mix}.

The NMR pulse sequence for $T_1 - T_2$ correlation measurements is shown in **Supplementary Figure 13a**. The sequence involves the measurement of a series of T_2 decays with differing degrees of T_1 encoding.[17] In this case a 2D ($n \times m$) data surface is obtained by acquiring the magnitude of n spin echoes encoded with $m \times \tau$ recovery delays, and a 2D distribution of T_1 and T_2 time constants is obtained via an inverse Laplace transform of this data. The acquired NMR data $S(nt_e, T_1, T_2)$ is again described by a Fredholm integral equation of the form[11]

$$S(nt_e, T_1, T_2) = S_0 \iint K(\tau, T_1, nt_e, T_2)\, F(T_1, T_2)\, d\log_{10}(T_1)\, d\log_{10}(T_2) + \epsilon(nt_e). \quad \textbf{(6)}$$

Here $F(T_1, T_2)$ and $\epsilon(nt_e)$ are the desired 2D distribution of T_1 and T_2 time constants and experimental noise, respectively, while the kernel function takes the form[15]

$$K(\tau, T_1, nt_e, T_2) = \left[1 - 2\exp\left(\frac{-\tau}{T_1}\right)\right]\exp\left(\frac{-nt_e}{T_2}\right). \quad \textbf{(7)}$$

The T_1 (indirect) dimension was encoded using 32 logarithmically spaced τ values ranging between 1 ms and 20 s, while the T_2 (direct) dimension was obtained by recording the magnitude of n = 30000 spin echoes. The 90° and 180° radio frequency pulse lengths were again 12.5 µs and 25 µs, respectively, and the echo time maintained at t_e = 250 µs. 8 repeat scans were used, taking 2 h to complete, and the recycle delay was 5 × T_1 of the slowest relaxing component. The (32 × 30000) data surface was inverted according to the methods described above, wherein the data was again smoothed according to the GCV method.

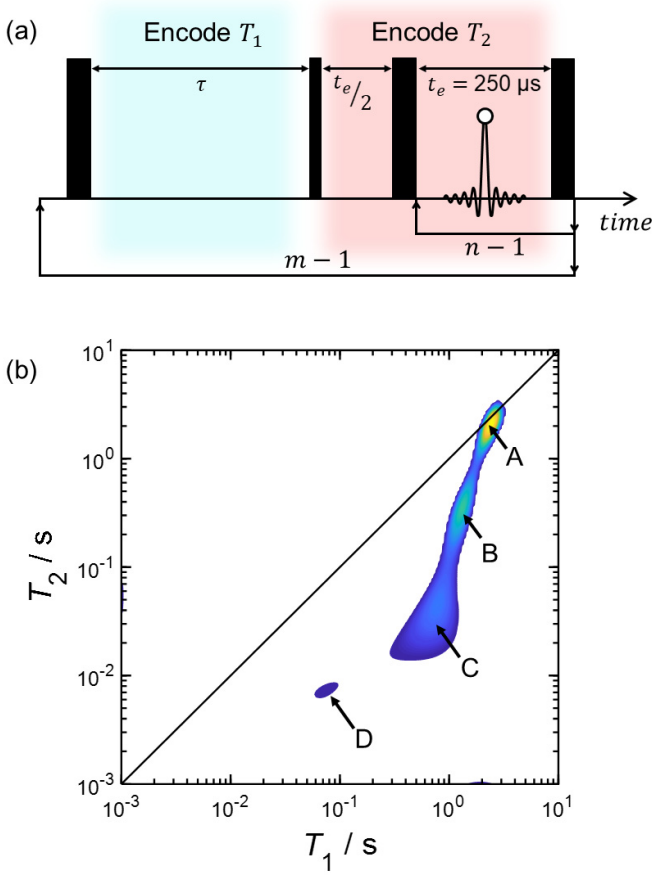

Supplementary Figure 13. (a) NMR pulse sequence for $T_1 - T_2$ correlation measurements. Thick and thin bars represent 180° and 90° radio frequency pulses, respectively. (b) Low-field ^{1}H $T_1 - T_2$ correlation data for unfunctionalised MM-SBA-15 in excess water. Peaks indicate the relative probability of the system exhibiting a given combination of T_1 and T_2 relaxation time constants. Peaks A, B, C and D are assigned to water populations: (A) outside the hierarchically porous framework, (B) within macropores, (C) within mesopores and (D) within micropores. Peak intensities follow the colour scheme defined in the main text.

Supplementary Table 4: Catalytic performance for cascade BDMA deacetalisation and Knoevenagel condensation.[a]

Catalyst	Average rate BDMA conversion / mmol.g_{cat}^{-1}.h^{-1}	6 h BDMA conversion / %	BCA yield / %
SZ/MgO/MM-SBA-15	945	99	68
Physical mixture	810	66	26
SZ/MM-SBA-15	966	100	8
MgO/MM-SBA-15	10	3	1
Blank	0	0	0

[a]Reaction conditions: 25 mg catalyst (except for physical mixture where 25 mg of each monofunctional catalyst was used), 5 mmol BDMA, 50 mmol ethyl cyanoacetate, 5 mmol deionised water, 5 cm^3 toluene, 1 mmol nonane as an internal standard, 50 °C under N_2.

[b]Calculated over first 10 min of reaction.

Supplementary Table 5: Catalytic performance for Knoevenagel condensation.[a]

Catalyst	Average rate / mmol.g_{cat}^{-1}.h^{-1}	6 h BZALD conversion / %	BCA yield / %
SZ/MgO/MM-SBA-15	240	81	72
Physical mixture	140	45	40
SZ/MM-SBA-15	40	16	16
MgO/MM-SBA-15	240	76	68
Blank	0	0	0

[a]Reaction conditions: 25 mg catalyst (except for physical mixture where 25 mg of each monofunctional catalyst was used), 5 mmol benzaldehyde, 50 mmol ethyl cyanoacetate, 5 mmol deionised water, 5 cm^3 toluene, 1 mmol nonane as an internal standard, 50 °C under N_2.

[b]Calculated over first 10 min of reaction.

Supplementary Note 1: Predicted BCA yield for physical mixture of SZ/MM-SBA-15 and MgO/MM-SBA-15.

The 6 h BCA yield from a physical mixture of SZ/MM-SBA-15 and MgO/MM-SBA-15 monofunctional catalysts, possessing the same number of acid and base sites respectively as SZ/MgO/MM-SBA-15 is predicted as follows:

The base catalyst alone was essentially inert towards BDMA deacetalisation whereas the acid catalyst alone achieved 100 % BDMA conversion over 6 h (**Supplementary Table 4**). Hence, for a 1:1 physical mixture of SZ/MM-SBA-15 and MgO/MM-SBA-15 catalysts, only BDMA molecules that encounter an acid catalyst particle will react. As the hierarchical silica frameworks of both catalysts are identical, we can assume that the probability of BDMA reacting to form benzaldehyde for the 1:1 physical mixture is therefore half of that for the acid catalyst alone, and hence the predicted BDMA conversion is 0.5×100 = 50 % over 6 h.

For the condensation step, the base catalyst alone converts 76 % of benzaldehyde to BCA whereas the acid catalyst alone only converts 16 % of benzaldehyde to BCA over 6 h (**Supplementary Table 5**). Hence for the 1:1 physical mixture of acid and base catalysts, the predicted benzaldehyde conversion to BCA is (0.5×76)+(0.5×16) = 46 %.

For the two-step cascade, the BCA yield from BDMA deacetalisation to benzaldehyde and subsequent condensation with ethyl cyanoacetate is predicted as the product of the individual steps (50 % × 46 %) = **23 %**, close to the experimentally observed BCA yield of 26 % for the physical mixture (**Supplementary Table 4**).

Supplementary References

1. Ecormier, M. A., Wilson, K. & Lee, A. F. Structure–reactivity correlations in sulphated-zirconia catalysts for the isomerisation of α-pinene. *J. Catal.* **215**, 57-65 (2003).
2. Osatiashtiani, A. *et al.* Hydrothermally stable, conformal, sulfated zirconia monolayer catalysts for glucose conversion to 5-HMF. *ACS Catal.* **5**, 4345-4352 (2015).
3. Callaghan, P. T. *Translational dynamics and magnetic resonance: principles of pulsed gradient spin echo NMR*. (Oxford University Press, 2011).
4. Barrie, P. J. in *Annual Reports on NMR Spectroscopy* Vol. 41 265-316 (Academic Press, 2000).
5. Mitchell, J., Chandrasekera, T. C., Johns, M. L., Gladden, L. F. & Fordham, E. J. Nuclear magnetic resonance relaxation and diffusion in the presence of internal gradients: The effect of magnetic field strength. *Phys. Rev. E* **81**, 026101 (2010).
6. Mitchell, J. & Chandrasekera, T. C. Understanding generalized inversions of nuclear magnetic resonance transverse relaxation time in porous media. *The Journal of Chemical Physics* **141**, 224201 (2014).
7. Washburn, K. E., Eccles, C. D. & Callaghan, P. T. The dependence on magnetic field strength of correlated internal gradient relaxation time distributions in heterogeneous materials. *Journal of Magnetic Resonance* **194**, 33-40 (2008).
8. Song, Y.-Q. Magnetic Resonance of Porous Media (MRPM): A perspective. *Journal of Magnetic Resonance* **229**, 12-24 (2013).
9. Kowalewski, J. & Maler, L. *Nuclear spin relaxation in liquids: theory, experiments, and applications*. (CRC press, 2017).
10. Monteilhet, L., Korb, J. P., Mitchell, J. & McDonald, P. J. Observation of exchange of micropore water in cement pastes by two-dimensional ${T}_{2}\text{\ensuremath{-}}{T}_{2}$ nuclear magnetic resonance relaxometry. *Physical Review E* **74**, 061404 (2006).
11. Washburn, K. E. & Callaghan, P. T. Tracking Pore to Pore Exchange Using Relaxation Exchange Spectroscopy. *Phys. Rev. Lett.* **97**, 175502 (2006).
12. Mitchell, J. *et al.* Validation of NMR relaxation exchange time measurements in porous media. *J. Chem. Phys.* **127**, 234701 (2007).
13. Mitchell, J., Chandrasekera, T. C. & Gladden, L. F. Numerical estimation of relaxation and diffusion distributions in two dimensions. *Prog. Nucl. Magn. Reson. Spectrosc.* **62**, 34-50 (2012).
14. Bernin, D. & Topgaard, D. NMR diffusion and relaxation correlation methods: New insights in heterogeneous materials. *Curr. Opin. Colloid Interface Sci.* **18**, 166-172 (2013).
15. Mitchell, J. *et al.* Determining NMR flow propagator moments in porous rocks without the influence of relaxation. *Journal of Magnetic Resonance* **193**, 218-225 (2008).
16. Hollingsworth, K. G. & Johns, M. L. Measurement of emulsion droplet sizes using PFG NMR and regularization methods. *J. Colloid Interface Sci.* **258**, 383-389 (2003).
17. Song, Y. Q. *et al.* T1–T2 Correlation Spectra Obtained Using a Fast Two-Dimensional Laplace Inversion. *J. Magn. Reson.* **154**, 261-268 (2002).